OPEN ACCESS
11th International Conference on New Frontiers in Physics
(ICNFP 2021)
International Journal of Modern Physics: Conference Series
Vol. 51 (2023) 2361005 (7 pages)

DOI: 10.1142/S2010194523610050

Recent SND experiment results on e^+e^- annihilation to hadrons

A. A. Korol*,†,‡, M. N. Achasov*,†, A. Yu. Barnyakov*, K. I. Beloborodov*,†, A. V. Berdyugin*,†, A. G. Bogdanchikov*, A. A. Botov*, T. V. Dimova*,†, V. P. Druzhinin*,†, L. V. Kardapoltsev*,†, A. G. Kharlamov*,†, D. P. Kovrizhin*, A. S. Kupich*, N. A. Melnikova*, A. E. Obrazovsky*, E. V. Pakhtusova*, K. V. Pugachev*,†, S. I. Serednyakov*,†, D. A. Shtol*, Z. K. Silagadze*,†, I. K. Surin*, Yu. V. Usov* and V. N. Zabin*

*Budker Institute of Nuclear Physics, Novosibirsk, 630090, Russia
†Novosibirsk State University, Novosibirsk, 630090, Russia
‡a.a.korol@inp.nsk.su

Published 27 December 2023

We review here recent results on e^+e^- annihilation to hadrons below 2 GeV obtained with the SND detector at the VEPP-2000 collider. Among others we report cross sections and dynamics properties for the $e^+e^- \to \pi^+\pi^-$, $e^+e^- \to n\bar{n}$, $e^+e^- \to \eta\pi^0\gamma$, and $e^+e^- \to \eta\eta\gamma$.

Keywords: e^+e^- annihilation; hadronic; cross-section; SND detector.

PACS numbers: 13.66.Bc, 14.40.Be, 13.40.Gp, 12.40.Vv

1. Introduction

SND[1–4] is an universal nonmagnetic detector including a tracking system (consisting of drift and proportional chambers in common gas volume), aerogel threshold Cherenkov counters, a three-layer electromagnetic calorimeter assembled from 1640 NaI(Tl) crystals, and a muon veto system (Fig. 1).

SND collected data at the VEPP-2000 e^+e^- collider[5] in the energy range 0.3–2.0 GeV in two runs, 2010–2013 and since 2017 up to now. Total integrated luminosity of about 370 pb^{-1} was recorded. The breakdown of integrated luminosity collected with detector by energy regions is shown in Table 1.

Main physics task of the SND experiment is the study of all possible processes of e^+e^- annihilation into hadrons below 2 GeV. In particular, these measurements are used to obtain the total hadronic cross section needed for Standard Model calculation of the anomalous magnetic moment of muon and running electromagnetic

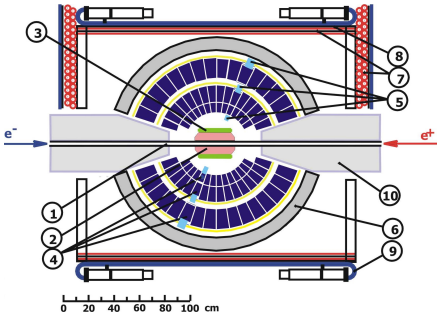

Fig. 1. SND layout: 1 — beam pipe, 2 — tracking system, 3 — aerogel Cherenkov counter , 4 — NaI(Tl) crystals, 5 — phototriodes, 6 — iron muon absorber, 7–9 — muon detector, 10 — focusing solenoids.

Table 1. The breakdown of integrated luminosity collected with detector by energy regions.

Energy range (GeV)	0.30–0.97	0.98–1.06	1.06–2.00
Integrated luminosity (pb^{-1})	77	31	259

coupling constant. A detailed study of dynamic of exclusive processes is also performed. In this report we present SND results on e^+e^- annihilation to the final states $\pi^+\pi^-$, $n\bar{n}$, $\pi^+\pi^-\pi^0$, $K^+K^-\pi^0$, $\eta\pi^0\gamma$, and $\eta\eta\gamma$.

2. The $e^+e^- \to \pi^+\pi^-$ Process

The process $e^+e^- \to \pi^+\pi^-$ is very important for calculation of the hadronic contribution to the $(g-2)$ of muon. There are many known measurements of this process cross-section. Some of them have systematic uncertainty less than 1%.

This measurement[6] is based on 4.6 pb^{-1} data collected in the energy 0.53–0.88 GeV, near 10 selection utilizes e/π separation based on the the three layer SND calorimeter data.[7] The measured $e^+e^- \to \pi^+\pi^-$ cross section is shown in Fig. 2 (left). The systematic uncertainty in the measurement is $\sim$ 0.8% in the energy range 0.6–0.9 GeV and $\sim$ 0.9% below 0.6 GeV. The result is fitted to the data with the vector-meson-dominance (VMD) model including the $\rho(770)$, $\omega(782)$, and $\rho(1450)$ resonances (Fig. 2, middle pane). The model describes data well, the obtained resonance parameters are in reasonable agreement with the previous SND[8] and other experiments[9] measurements.

Thois cross section measurement of the $e^+e^- \to \pi^+\pi^-$ is in agreement with the previous energy-scan measurements performed at the VEPP-2M collider with the CMD-2[10] and SND[8] detectors. The comparison of the fit to the SND data with the currently most accurate BABAR[11] and KLOE[12] measurements performed using the initial-state radiation technique the initial-state radiation technique is presented in Fig. 2 (middle systematic differences between the SND and BABAR data below 0.7 GeV and between the SND and KLOE data above 0.7 GeV.

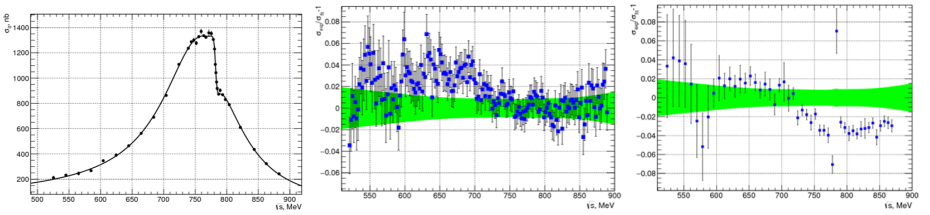

Fig. 2. The $e^+e^- \to \pi^+\pi^-$ cross section measured by SND (left pane). The curve is the result of the VMD fit. The relative difference between the BABAR[11] (middle pane) and KLOE[12] (right pane) $e^+e^- \to \pi^+\pi^-$ data and the SND fit. The band represents the statistical and systematic uncertainties of the SND fit combined in quadrature.

The contribution to the muon anomalous magnetic moment from the $e^+e^- \to \pi^+\pi^-$ channel in the energy region 0.53–0.88 GeV calculated from this cross-section measurement is $(409.8 \pm 1.4 \pm 3.9) \times 10^{-10}$. This value is in good agreement with the values obtained using the previous results: $(406.5 \pm 1.7 \pm 5.3) \times 10^{-10}$ for SND,[8] $(413.6 \pm 2.0 \pm 2.3) \times 10^{-10}$ for BABAR,[11] and $(403.4 \pm 0.7 \pm 2.5) \times 10^{-10}$ for KLOE.[12]

3. The $e^+e^- \to n\bar{n}$ Process

The process $e^+e^- \to n\bar{n}$ was previously measured by FENICE,[13] and SND[14] using the 2011-2012 data set. The new SND measurement was based on 2017 and 2019 data and used a different method of signal-background separation compared with Ref. 14.

For 2017 data, we analyze the distribution of the time difference between the calorimeter trigger signal and the beam revolution synchronization signal. This difference is measured with a rather poor resolution of about 6 ns. In the 2019 run, the time measurement technique in the calorimeter was significantly improved.[15] For each calorimeter crystal, the signal from the photodetector shaped with integration time of about 1 μs was digitized with flash ADC at sampling rate $\sim$ 36MHz. The signal amplitude and its arrival time were fitted with a fixed calibrated signal shape. Then the event time was calculated as a weighted average of crystal arrival times using the energy deposition used as a weight. The time resolution measured for $e^+e^- \to \gamma\gamma$ events was $\sim$ 0.8 ns, nearly an order of magnitude better than one for the 2017 run.

The time distributions for selected data events of the 2019 run at $E = 1.89$ GeV and 1.95 GeV are shown in Fig. 3. The time distribution consists of the nearly uniform cosmic-ray distribution, the distribution for the beam-induced and physical backgrounds, which is peaked near zero, and a wide $n\bar{n}$ distribution, which is shifted relative to other e^+e^- annihilation events due to small antineutron velocity. From the fit to data with the sum of all three distributions we were able determine the number of $n\bar{n}$ events. The shape of the beam-induced and physical background distribution was measured using data recorded below the $n\bar{n}$ threshold.

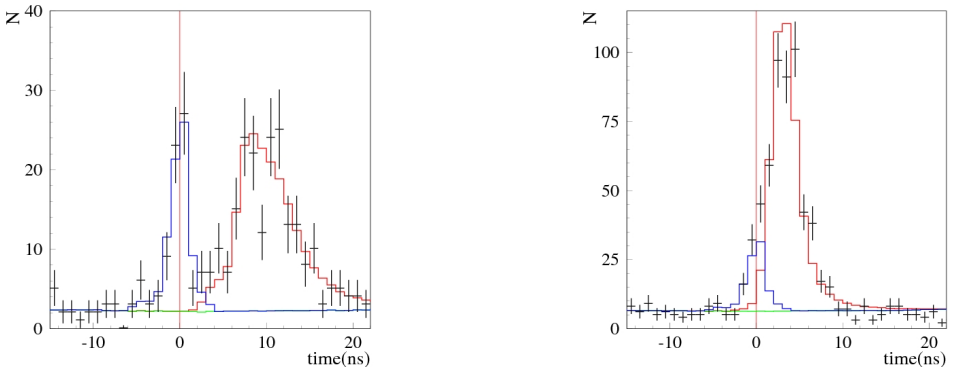

Fig. 3. The time distribution for selected data events collected in 2019 (points with error bars) at $E = 1.89$ GeV (left pane) and 1.95 GeV (right pane). The blue histogram is the fitted sum of the cosmic-ray, beam-induced and physical backgrounds contributions, and fitted $n\bar{n}$ signal.

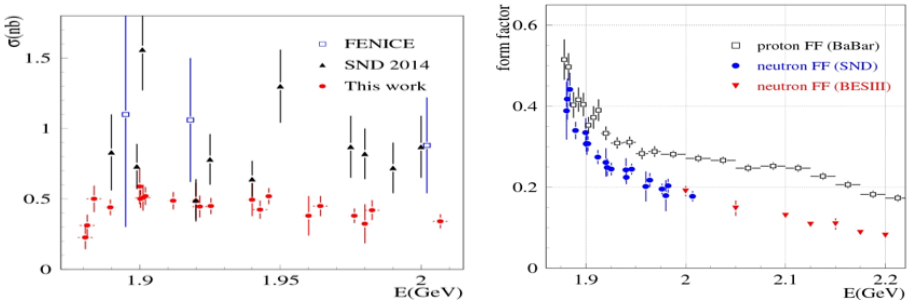

Fig. 4. Left panel: The preliminary SND results on the $e^+e^- \to n\bar{n}$ cross section (solid circles) compared with the previous FENICE[13] (empty squares) and SND[14] (filled triangles) measurements. Only statistical error are shown. Right panel: The SND preliminary result on the neutron effective form factor (circles), compared with the BESIII[17] neutron form factor (stars) and the proton form factor measured by BABAR[16] (empty squares).

Our preliminary results on the $e^+e^- \to n\bar{n}$ cross section are shown in Fig. 4 (left). The statistical accuracy of the measurement is significantly improved compared with the previous SND measurement.[14] However the new SND result is systematically lower than the previous one by about 30% at 1.9 GeV and by two times near 2 GeV. The main reasons were underestimated beam background and not quite accurate MC simulation in the previous measurement. The systematic uncertainty on the cross section is measurement. The systematic uncertainty on the cross section is estimated to be about 15

The $e^+e^- \to n\bar{n}$ cross section depends on magnetic and electric form factors. From the measured cross section we determine the so-called effective form factor, which is shown in Fig. 4 (right) in comparison with with the BESIII measurement of the neutron form factor[17] above 2 GeV and the BABAR measurement of the

Table 2. Preliminary SND results on the $|G_E/G_M|$ ratio.

Energy range (GeV)	1.89–1.902	1.91–1.925	1.95–1.975
$\lvert G_E/G_M\rvert$	0.77 ± 0.27	1.34 ± 0.33	1.70 ± 0.53

proton form factor.[16] The SND and BESIII results near 2 GeV are in agreement. The proton and neutron effective form factors are close to each other in the near-threshold region. The difference between them grows with increase of the energy.

The ratio of the form factors can be determined from the analysis of the antineutron polar angle distribution. The results of the fit to the angular distribution for the 2019 data set in three energy regions are listed in Table 2. Our preliminary results agree with the assumption that $|G_E/G_M| = 1$, but also do not contradict larger values $|G_E/G_M| \approx 1.4$–1.5 observed in the BABAR[16] and BESIII[18] experiments for the ratio of proton form factors near $E = 2$ GeV.

4. The $e^+e^- \to \pi^+\pi^-\pi^0\gamma$ and $e^+e^- \to K^+K^-\pi^0\gamma$ Processes

These two processes were analyzed using data with an integrated luminosity of 35 pb^{-1} collected in 2011–2012. In the energy region 1.15–2.0 GeV we study the dynamics of the process $e^+e^- \to \pi^+\pi^-\pi^0$.[19] The energy region was divided into 14 intervals. For each interval, the Dalitz plot distribution and $\pi^+\pi^-$ mass spectrum were fitted by the model containing a sum of amplitudes for the three intermediate states: $\rho(770)\pi$, $\rho(1450)\pi$, and $\omega\pi^0$. The results of the fit are presented in Fig. 5 (left), where the fitted cross section for the intermediate states are shown together with the total $e^+e^- \to \pi^+\pi^-\pi^0$ cross section. One can see that the cross section for $\rho(1450)\pi$ ($\sigma_{\rho'\pi}$) differs from zero in the region of the second maximum in the

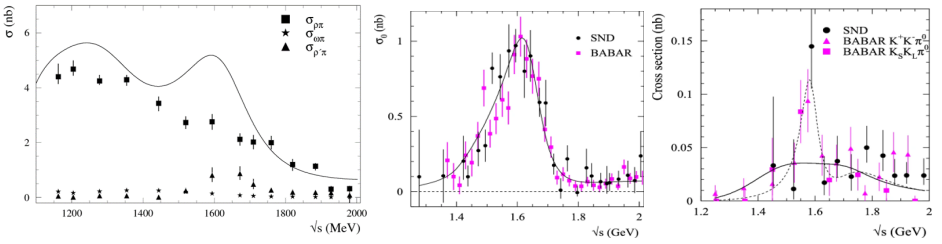

Fig. 5. Left panel: The measured energy dependences of the cross sections for the intermediate states $\rho(770)\pi$, $\rho(1450)\pi$, and $\omega\pi^0$. The curve is the result of the VMD fit to the SND data on the total $e^+e^- \to \pi^+\pi^-\pi^0$ cross section. Middle panel: The $e^+e^- \to K^+K^-\pi^0$ cross section measured by SND (circles) compared with the BABAR[21] data (squares). The curve is the result of the VMD fit with the $\phi(1020)$ and $\phi(1680)$ resonances. Right panel: The $e^+e^- \to \phi\pi^0 \to K^+K^-\pi^0$ cross section measured by SND in comparison with the two BABAR measurements.[21,22] The solid curve represents the VMD fit to the SND and BABAR data with the $\rho(1450)$ and $\rho(1700)$ resonances, while the dashed curves is the result of the same fit with free parameters of the first resonance.

$e^+e^- \to \pi^+\pi^-\pi^0$ cross section, corresponding to the $\omega(1650)$ resonance. In the cross section for $\rho(770)\pi$ ($\sigma_{\rho\pi}$), clear resonance structure near 1650 MeV is absent.

We conclude that the intermediate state $\rho(1450)\pi$ gives a significant contribution to the decay of $\omega(1650) \to \pi^+\pi^-\pi^0$, while the $\rho(770)\pi$ dominates in the $\omega(1420) \to \pi^+\pi^-\pi^0$ decay. The difference between the total cross section and the sum of the three cross sections for the intermediate states is due to interference.

The $e^+e^- \to K^+K^-\pi^0$ process below 2 GeV proceeds predominantly through the $K^*(892)^\pm K^\mp$ intermediate state, but the signal from the $\phi\pi^0$ intermediate state is also seen. The cross sections for the process $e^+e^- \to K^+K^-\pi^0$ (without $\phi\pi^0$) and $e^+e^- \to \phi\pi^0 \to K^+K^-\pi^0$ were measured separately.[20] The measured cross sections shown in Fig. 5 (middle and right) agree well with the previous measurements in the BABAR experiment[21,22] and have comparable accuracy. In the narrow region near $\sqrt{s} = 1.58$ GeV all three existing measurements of the $e^+e^- \to \phi\pi^0$ cross section [see Figure 5(right)] show excess over the model including known vector resonances. This excess can be interpreted as a contribution of the resonance with $M = 1585 \pm 15$ MeV and $\Gamma = 75 \pm 30$ MeV. This contribution significance is estimated at a level of about 3σ.

5. Radiative processes $e^+e^- \to \eta\pi^0\gamma$ and $e^+e^- \to \eta\eta\gamma$

The processes $e^+e^- \to \eta\pi^0\gamma$[23] and $e^+e^- \to \eta\eta\gamma$[26] above 1.05 GeV were measured for the first time. They were studied in the five-photon final state.

In the process $e^+e^- \to \eta\pi^0\gamma$ there is a significant contribution of the $\omega\eta$ intermediate state, which is seen as a peak at ω mass value in the $\pi^0\gamma$ mass distribution. The non-$\omega\eta$ signal is also present. It may arise from the processes $e^+e^- \to a_0(1450)\gamma$ and $a_2(1320)\gamma$. Figure 6 (left) shows the measured $e^+e^- \to \omega\eta$ cross section in comparison with the SND and CMD-3 measurements in the decay mode $\omega \to 3\pi$, while Fig. 6 (middle) represents the first measurement of the non-$\omega\eta$ part of the $e^+e^- \to \eta\pi^0\gamma$ cross section.

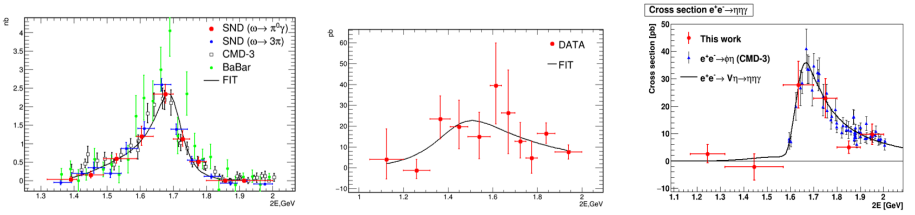

Fig. 6. The $e^+e^- \to \omega\eta$ cross section measured by SND in the $\eta\pi^0\gamma$ final state in comparison with the SND[24] and CMD-3[25] measurements in the $\pi^+\pi^-\pi^0\eta$ final state (left pane). The non-$\omega\eta$ $e^+e^- \to \eta\pi^0\gamma$ cross section measured by SND (middle pane). The the $e^+e^- \to \eta\eta\gamma$ cross section (right pane) measured by SND (circles) compared with the $e^+e^- \to \phi\eta$ cross section measured by CMD-3 in the decay mode $\phi \to K^+K^-$[27] (triangles). The solid curve is the sum of the $e^+e^- \to \phi\eta$, $\rho\eta$ and $\omega\eta$ cross sections.

The dominant intermediate state in the process $e^+e^- \to \eta\eta\gamma$ is $\phi\eta$. The measured cross section shown in Fig. 6 (right) is consistent with the CMD-3 result on $e^+e^- \to \phi\eta$ obtained in the decay mode $\phi \to K^+K^-$. The contribution from intermediate states other than $\phi\eta$ is not seen. The upper limits are set on a possible contribution of radiative intermediate states as $f_0(1500)\gamma$ or $f_2'(1525)\gamma$. In the energy range of the $\rho(1700)$ and $\phi(1680)$ resonances the limit is 11 pb at 90% confidence level.

Acknowledgments

This work is supported in part by the RFBR grants 20-02-00060 and 20-02-00347.

References

1. M. N. Achasov *et al.*, *Nucl. Instrum. Methods Phys. Res., Sect. A* **598** (2009) 31.
2. V. M. Aulchenko *et al.*, *Nucl. Instrum. Methods Phys. Res., Sect. A* **598** (2009) 102.
3. A. Y. Barnyakov *et al.*, *JINST* **9** (2014) C09023.
4. V. M. Aulchenko *et al.*, *Nucl. Instrum. Methods Phys. Res., Sect. A* **598** (2009) 340.
5. A. Romanov *et al.*, in *Proceedings of Particle Accelerator Conference PAC 2013, Pasadena, CA USA, 2013*, p. 14.
6. M. N. Achasov *et al.* (SND Collaboration), *JHEP* **1** (2021) 113.
7. M. N. Achasov and A. S. Kupich, *JINST* **12** (2017) C06035.
8. M. N. Achasov *et al.* (SND Collaboration), *J. Exp. Theor. Phys.* **103** (2006) 380.
9. M. Tanabashi *et al.* (Particle Data Group), *Phys. Rev. D* **98** (2018) 010001.
10. R. R. Akhmetshin *et al.* (CMD-2 Collaboration), *Phys. Lett. B* **648** (2007) 28.
11. J. P. Lees *et al.* (BaBar Collaboration), *Phys. Rev. D* **86** (2012) 032013.
12. A. Anastasi *et al.* (KLOE Collaboration), *JHEP* **3** (2018) 173.
13. A. Antonelli *et al.* (FENICE Collaboration), *Nucl. Phys. B* **517** (1998) 3.
14. M. N. Achasov *et al.* (SND Collaboration), *Phys. Rev. D* **90**(11) (2014) 112007.
15. M. N. Achasov *et al.*, *JINST* **10** (2015) T06002.
16. J. P. Lees *et al.* (BaBar Collaboration), *Phys. Rev. D* **87** (2013) 092005.
17. M. Ablikim *et al.* (BESIII Collaboration), arXiv:2103.12486 [hep-ex].
18. M. Ablikim *et al.* (BESIII Collaboration), *Phys. Rev. Lett.* **124** (2020) 042001.
19. M. N. Achasov *et al.* (SND Collaboration), *Eur. Phys. J. C* **80** (2020) 993.
20. M. N. Achasov *et al.* (SND Collaboration), *Eur. Phys. J. C* **80** (2020) 1139.
21. B. Aubert *et al.* (BABAR Collaboration), *Phys. Rev. D* **77** (2008) 092002.
22. J. P. Lees *et al.* (BABAR Collaboration), *Phys. Rev. D* **95** (2017) 052001.
23. M. N. Achasov *et al.* (SND Collaboration), *Eur. Phys. J. C* **80** (2020) 1008.
24. M. N. Achasov *et al.* (SND Collaboration), *Phys. Rev. D* **99** (2019) 112004.
25. R. R. Akhmetshin *et al.* (CMD-3 Collaboration), *Phys. Lett. B* **773** (2017) 150.
26. M. N. Achasov *et al.* (SND Collaboration), arXiv:2110.05845 [hep-ex].
27. V. L. Ivanov *et al.* (CMD-3 Collaboration) *Phys. Lett. B* **798** (2019) 134946.